Chinese Journal of
POLYMER SCIENCE

RESEARCH ARTICLE

https://doi.org/10.1007/s10118-025-3288-8
Chinese J. Polym. Sci. **2025**, *43*, 605–615

Investigating the Influence of Printing Parameters on the Helical Deformation of 4D-printed Liquid Crystal Elastomer Fiber-actuators

Chun Zhang[a,b,†], Reyihanguli Muhetaer[b,†], Tong-Zhi Zang[b,c], Shuang Fu[b], Jun-Peng Cheng[b], Li Yang[a], Jian Wang[a], Kun Yang[a], Guo-Xia Fei[b*], Qing-Yuan Wang[a*], Xi-Li Lu[b*], He-Sheng Xia[b*], and Yue Zhao[d]

[a] *Institute for Advanced Study, Chengdu University, Chengdu 610106, China*
[b] *National Key Laboratory of Advanced Polymer Materials, Polymer Research Institute, Sichuan University, Chengdu 610065, China*
[c] *Center for Molecular Science and Engineering, College of Science, Northeastern University, Shenyang 110819, China*
[d] *Département de chimie, Université de Sherbrooke, Sherbrooke, Québec J1K 2R1, Canada*

Electronic Supporting Information

Abstract Liquid crystal elastomers (LCEs) exhibit exceptional reversible deformation and unique physical properties owing to their order-disorder phase transition under external stimuli. Among these deformations, helical structures have attracted attention owing to their distinctive configurations and promising applications in biomimetics and microelectronics. However, the helical deformation behavior of fiber actuators is critically influenced by their morphologies and alignments; yet, the underlying mechanisms are not fully understood. Through a two-step aza-Michael addition reaction and direct ink writing (DIW) 4D printing technology, fiber-based LCE actuators with a core-sheath alignment structure were fabricated and exhibited reversible helical deformation upon heating. By adjusting the printing parameters, the filament number, width, thickness, and core-sheath structure of the fiber actuators can be precisely controlled, resulting in deformation behaviors, such as contraction, bending, and helical twisting. Finite element simulations were performed to investigate the deformation behaviors of the fiber actuators, providing insights into the variations in stress and strain during the shape-changing process, which can be used to explain the shape-morphing mechanism. These findings demonstrate that the precise tuning of printing parameters enables the controllable construction of LCE actuator morphology and customization of their functional properties, paving the way for advanced applications in smart fabrics, biomedical engineering, and flexible electronics.

Keywords Liquid crystal elastomer; 4D printing; Helical deformation; Finite element simulation; Fiber actuators

Citation: Zhang, C.; Muhetaer, R.; Zang, T. Z.; Fu, S.; Cheng, J. P.; Yang, L.; Wang, J.; Yang, K.; Fei, G. X.; Wang, Q. Y.; Lu, X. L.; Xia, H. S.; Zhao, Y. Investigating the influence of printing parameters on the helical deformation of 4D-printed liquid crystal elastomer fiber-actuators. *Chinese J. Polym. Sci.* **2025**, *43*, 605–615.

INTRODUCTION

Liquid crystal elastomers (LCEs) are known for their excellent reversible deformations and unique physical properties.[1–3] Under external stimuli, LCEs can undergo rapid and large-scale reversible deformations due to the order-disorder phase transition associated with the orientation of the mesogens, exhibiting high controllability and responsiveness. These distinctive properties make LCEs promising for a range of advanced applications including soft robots,[4,5] actuators,[6,7] artificial muscles,[8–10] and biomedical devices.[11,12]

4D printing technology, which introduces the dimension of time to enable 3D printed structure transformation in response to external stimuli, has garnered significant attention in fields such as soft robotics, smart materials, and biomedical research.[13–15] In recent years, researchers have integrated LCE actuators with 4D printing, simplifying the fabrication process and enabling precise control over both mesogen alignment and macroscopic geometry.[16–18] Among the various 4D printing techniques, direct ink writing (DIW) has become the most widely used method for the fabrication of LCE actuators because of its high material compatibility and printing flexibility.[19–22] During the DIW process, the liquid crystal (LC) ink is extruded through a nozzle and deposited along predefined paths onto the printing platform. During extrusion, shear and extensional forces induced mesogen alignment along the printing path. Thus, the mesogen alignment can be precisely adjusted by controlling the printing path, offering predetermined and pre-programmed shape morphing

* Corresponding authors, E-mail: feiguoxia@scu.edu.cn (G.X.F.)
E-mail: wangqy@scu.edu.cn (Q.Y.W.)
E-mail: xililu@scu.edu.cn (X.L.L.)
E-mail: xiahs@scu.edu.cn (H.S.X.)
† These authors contributed equally to this work.
Special Topic: Smart Elastomers and Actuators
Received November 26, 2024; Accepted January 7, 2025; Published online February 24, 2025

of the responsive materials. As a result, various unique alignment structures can be constructed, exhibiting a variety of deformations such as bending,[23, 24] curling,[25] or twisting.[26–28] 3D helical structures can be found in climbing plants that use helical tendrils to elevate themselves for sunlight acquisition (Fig. 1a). Tendril coiling arises from asymmetric contractions of the fiber ribbon, where the ventral side contracts longitudinally compared to the dorsal side, resulting in the intrinsic curvature.[29] These unique mechanical properties and versatility make such structures highly attractive for a wide range of applications in biomimetics and technology, such as microelectronics[30–32] and microactuators[33]

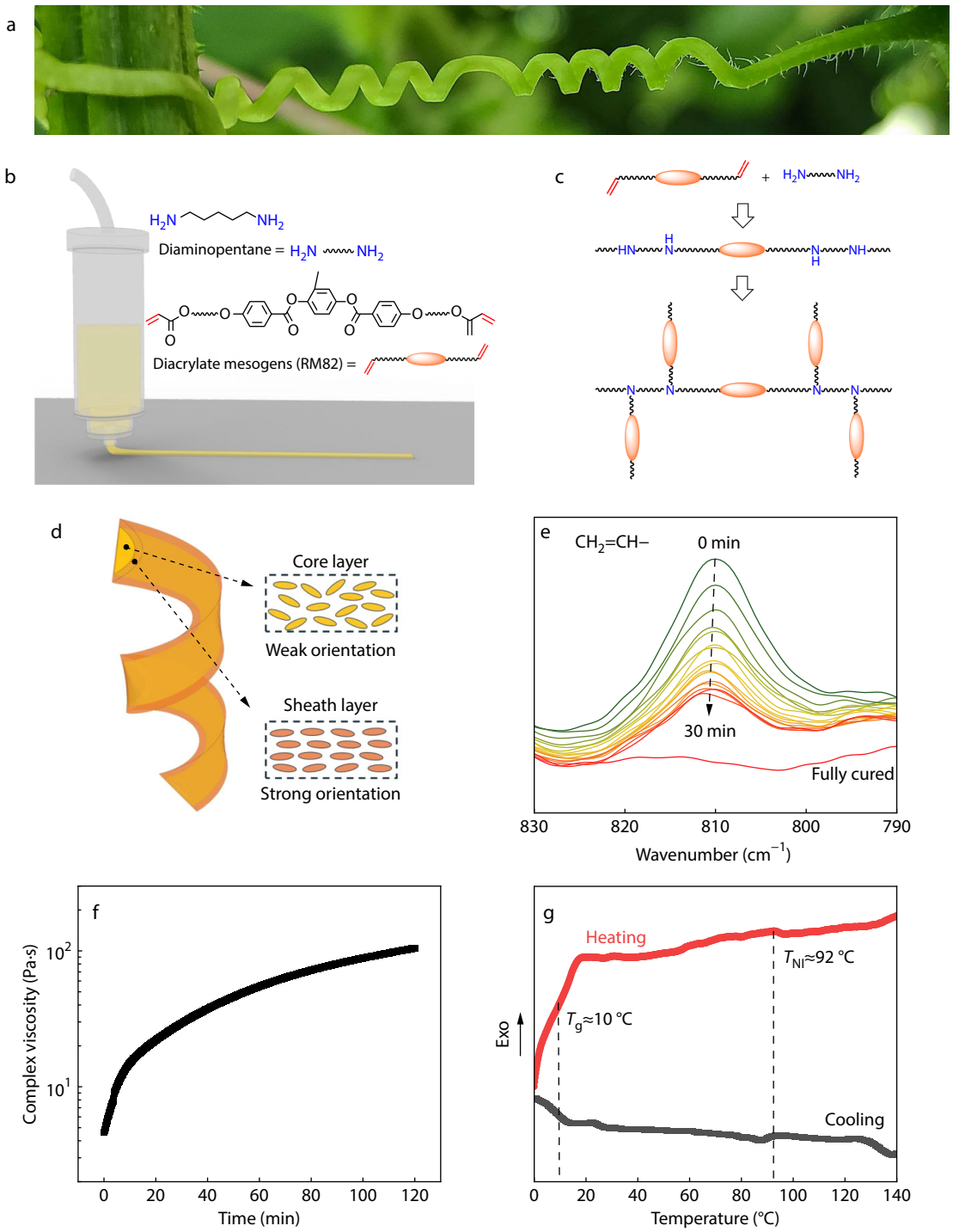

Fig. 1 (a) The image of a cucumber plant tendril with helix structure. (b) Schematic illustration of the printing process of the LCE fibers. (c) Two-step crosslinking reaction of the LC ink. (d) Illustration of the asymmetric core-sheath structure of fiber actuator. (e) Fourier transform infrared (FTIR) spectra monitoring the acrylate conversion during the reaction. (f) Changes of complex viscosity of the ink with time at 50 °C. (g) The DSC heating curves of the printed LCE fiber.

https://doi.org/10.1007/s10118-025-3288-8

and artificial muscles.[34]

Precise control of helical transformations is crucial for the development of reliable and efficient devices.[35] The *Bauhinia* seed pod undergoes a flat-to-helical transition when exposed to changes in humidity. Armon *et al.*[36] studied this helical transition using strips cut from composite elastic materials that mimic the structure of the pod valve tissue. They found that the variety of helical shapes is controlled by two dimensionless parameters: the direction θ between the strip's long axis and the directions of the intrinsic curvature (*i.e.*, the fiber directions), and a dimensional parameter containing the width, thickness, and intrinsic curvature of the strip. Sawa *et al.*[37] performed experiments on strips composed of twist-nematic elastomer films. The results showed that films with a small width-to-thickness ratio were easier to stretch and form helicoids, whereas those with a large width-to-thickness ratio were easier to bend and form spiral ribbons. The pitch and handedness of the formed ribbons were determined based on temperature and width-to-thickness ratio. Lu *et al.*[38] investigated the twisting motion of chiral liquid crystalline elastomer strips and revealed that fiber-like strips with a high aspect ratio (length/width) are more likely to form a spring-like structure. In addition, the thickness of the strip has a significant effect on twisting deformation. As the thickness increased, both the helical pitch and diameter increased, suggesting greater resistance to twisting deformation.

In our previous work, we utilized DIW 4D printing to fabricate LCE artificial tendrils with asymmetric core-sheath structures. Owing to their asymmetric contraction behavior, the fibers exhibited reversible helical deformation under thermal stimulation, and the deformation mechanism was clarified through finite element simulations.[39] However, the aspect ratio and orientation characteristics of fiber actuators play a crucial role in the helical deformation behavior, which has not yet been fully understood. In this study, based on our previous research, we controlled the printing parameters to fabricate LCE fiber actuators with distinct morphologies and orientations, and explored the effects of different aspect ratios and orientation structures on the helical deformation behavior of fiber actuators.

EXPERIMENTAL

Materials

The LC monomer 1,4-bis-[4-(6-acryloyloxyhexyloxy) benzoyloxy]-2-methylbenzene (RM82, 98%) was purchased from Beijing Bayi Space Time LCD Technology Co., Ltd. 1,5-Diaminopentane (98%) served as chain extender, and crosslinker was purchased from Adamas. All the reagents and solvents were used without further purification.

Preparation of the LCE Fibers

The LCE fibers were obtained *via* a two-step reaction between the diacrylate monomers and diamines *via* aza-Michael addition. In the initial phase, a prepolymer containing mesogenic units was synthesized. A mixture of RM82 (0.168 g), 1,5-diaminopentane (0.023 g), and dimhylformamide (DMF, 0.020 g) was loaded into a glass vial. The mixture was heated and homogenized using a heat gun and mixer (Thinky Corporation, AR-100) to form an LC ink suitable for printing. Subsequently, the ink was transferred into the syringe of a commercial 3D bioprinter (Regenovo, Bio-Printer-WS), with printer settings finely tuned to an extrusion temperature of 50 °C and a substrate temperature of 15 °C. Under nitrogen atmosphere, the ink was extruded through nozzles of varying diameters. The nozzles deposited the LC ink layer by layer along a predetermined trajectory to fabricate a three-dimensional structure. The printed samples were subjected to 24-h post-treatment in a vacuum oven at 85 °C to facilitate the secondary crosslinking reaction for fixation of the oriented structure and evaporation of the solvent.

Characterization

The LC ink was analyzed using a Fourier transform infrared spectrometer (Nicolet iS50, Thermo Fisher Scientific) to monitor the acrylate conversion. The test samples included both the LC oligomer inks and fully cured thin films. The rheological properties of the ink were characterized using a strain-controlled rheometer (ARES G2, TA Instruments) to assess viscosity variation over time. By employing a parallel plate configuration with a diameter of 25 mm and a gap of 0.2 mm, The test was conducted at a constant frequency of 50 Hz and a stress level of 5%. The test plates were equilibrated at 50 °C before ink was introduced for standardized analysis. The phase transition temperatures of the LCE were determined using differential scanning calorimetry (DSC, Q2000, TA Instruments). The analysis was conducted over a temperature range of 0–150 °C under a nitrogen atmosphere, with a flow rate of 50 mL·min^{-1} and a heating rate of 5 °C·min^{-1}. Dynamic mechanical analysis (DMA) was performed on a DMA Q800 apparatus (TA Instruments) in tension film mode. Rectangular geometry samples [*ca.* 0.3 mm (T) × 2 mm (W) × 10 mm (L) and a gauge length of ~8 mm] were measured from −10 °C to 150 °C at a heating rate of 3 °C·min^{-1}, under a strain of 0.2% and frequency of 1 Hz. The mesophase texture and orientation of the printed LCE fibers were examined using a polarizing optical microscope (POM) equipped with cross-polarizers (LV100-POL, Nikon).

Finite Element Simulation

The detail of finite element modeling details The 3D FE model ABAQUS/Dynamic, Temperature-displacement, and Explicit quasi-static analyses were used to reveal the deformation mechanism and energy dissipation of the LCE artificial tendril during heating. The model was meshed using a C3D8RT element (an 8-node thermally coupled brick, trilinear displacement and temperature, reduced integration, hourglass control). The mesh size is approximately 0.02 mm and the total number of elements of each model is approximately 6×10^4. The prescribed conditions include the following: the entire fiber is subjected to gravity, one end of the fiber is completely fixed, and a certain initial temperature. General contact interactions are defined to simulate possible self-contact. The temperature change of materials is realized by specifying different environmental temperatures (sink temperature: 20–140 °C) and heat transfer coefficient [film coefficient: 0.25 W (mm^2 ·°C)]. The parameters of the finite element analysis (FEA) model and coefficient of thermal expansion (α) in the x, y, and z directions are listed in Tables S1 and S2 (in the electronic supplementary information, ESI). To simplify the model, the thermal conductivity, Poisson's ratio, density, and specific heat capacity were set as the isotropic and temperature-independent parameters. The dimensional parameters of the models, including the length, width, and thickness,

https://doi.org/10.1007/s10118-025-3288-8

are listed in Tables S3, S4, S5, S6, S7, and S8 in the ESI.

RESULTS AND DISCUSSION

This study investigated the influence of dimensional parameters on the asymmetric deformation of LCE fibers. The LCE fibers were fabricated using a two-step aza-Michael addition reaction, with RM82 as the LC monomer, 1,5-diaminopentane as the chain extender and crosslinker, and DMF as the solvent, using the DIW 4D printing technique (Fig. 1b). The reaction occurs as primary hydrogen atoms participate in the addition reaction, whereas secondary hydrogen atoms engage in the reaction only after the primary hydrogen atoms are fully consumed, thereby forming a crosslinked network structure (Fig. 1c). Fig. 1(d) shows the asymmetric core-sheath structure of the fiber actuator. The changes in the chemical structure during the printing process were investigated using temperature-dependent (*in situ*) FTIR spectroscopy. As shown in Fig. 1(e), the peak intensity of the double bond at 810 cm^{-1} decreased within 30 min, indicating a chain extension reaction of the LC ink during the printing process. After treatment at 80 °C for 24 h, the disappearance of the double bond peak suggests the complete curing of the LCE fibers.

During this process, the rheological properties changed accordingly. To investigate the rheological behavior of the LC ink during printing, strain-controlled rheological testing was conducted at 50 °C. As the aza-Michael addition reaction proceeded, LC oligomers were formed and the gap between G' and G'' radually decreased, as shown in Fig. S2 (in ESI). When G' exceeds G'', it indicates that the ink has transitioned from a flow state to a gel state that can no longer be extruded. During this process, the complex viscosity also increases gradually, as shown in Fig. 1(f). The kinetic difference between the primary and secondary hydrogen atoms creates an advantageous window for the printing process. During the extrusion process, the shear force generated by the nozzle and the tension force in motion induced regular alignment of the LC mesogens along the print direction. Throughout the printing process, the viscosity of the ink increased gradually as a result of the ongoing chain elongation and crosslinking reactions. Therefore, the nitrogen pressure was dynamically adjusted to ensure the continuity and integrity of the printing process. The printed fibers exhibited a glass transition at approximately 10 °C (T_g) and an ordered nematic phase to a disordered isotropic phase transition at approximately 92 °C (T_{NI}), as shown in the DSC test in Fig. 1(g).

The typical response mechanism of an LCE actuator involves a thermoresponsive shape change. As the temperature exceeds T_{NI}, the mesogen transitions from an ordered-to-disordered state, leading to macroscopic deformation of the LCE material. When the temperature decreases below T_{NI}, the mesogens return to their original ordered state, allowing the material to recover its initial shape. In this work, LCE actuators with a high aspect ratio (from single- to multi-fiber) underwent helical deformation upon heating owing to the asymmetric contraction of the core-sheath structure. This unique deformation behavior is related to the macroscopic dimensions of the LCE actuators (width and thickness) as well as the alignment of the core-sheath structure. To investigate the effects of various dimensional parameters on the deformation of the LCE actuators (single- and multi-fibers), a series of rationally designed experiments were conducted. Throughout these experiments, critical printing parameters, including the printing speed, printing time, and nozzle-to-substrate distance, were controlled. A diverse array of fibers characterized by varying widths, thicknesses, and core-sheath structures was fabricated. Subsequently, the thermally induced deformations of these actuators were recorded with videos, and the mechanism of helical deformation was investigated using theoretical models and finite element simulations.

To investigate the effect of the printing width on the deformation of LCE actuators, we employed DIW 4D printing to fabricate samples of varying widths (from single- to multi-filaments) using a 0.34 mm (24G) nozzle at a constant printing speed of 5 mm/min. The printed samples consisted of different numbers of filaments (1, 5, 10, and 20), and each filament exhibited a core-sheath structure, as shown in Figs. 2(a) and 2(b). Fig. 2(c) presents POM images and cross-sectional views of the samples containing (i) 1, (iii) 5, and (iv) 10 filaments. Owing to the birefringence of the LC phase, a 45° rotation of the actuators results in a transition between bright and dark fields, indicating that the printed actuators form a well-oriented structure along the printing direction. All the samples exhibited a similar thickness and semi-elliptical cross-sectional shape. Residual stress exists within the extruded filaments, leading to an increase in the curvature of the as-printed samples as the number of filaments increases. When the samples were placed near a vertically standing hot plate at approximately 160 °C, the sample with a single filament transitioned from its initial vertical state to a uniform and tight coil state (Fig 2d i). The sample containing five filaments also formed a helical shape; however, only a single helical turn was observed (Fig. 2d ii). For the samples with 10 and 20 filaments, significant bending deformation was observed in the as-printed actuators (Fig. 2d iii and iv). These samples first bend in the opposite direction and finally form a helix or coil upon heating, and rapidly return to their original shapes upon cooling (Video S1 in ESI). This result indicates that as the printing width increases, that is, as the aspect ratio decreases, the helical deformation of the actuators gradually transitions into a coiling or even bending deformation. It should be emphasized that, during printing and chemical crosslinking, the molecular chains in the sheath and core layers undergo varying degrees of shearing, orientation, and relaxation. The internal stresses fixed by chemical crosslinking in different fiber actuators lead to different initial shapes. While the initial shape may affect the early stage deformation (such as curvature or shape-morphing rate), the final deformation state is determined by the 3D orientation structure of the actuators and the different contraction forces and strains induced by the sheath-core structure (as demonstrated by finite element simulations).

Through finite element simulation, we studied the deformation process of the fibers with temperature and stress distributions in the deformed structures. The heat transfer coefficient α value and specific dimensional parameters of the printed samples can be found in Tables S2 and S3 in ESI. The FEA models varied in width and were composed of different

https://doi.org/10.1007/s10118-025-3288-8

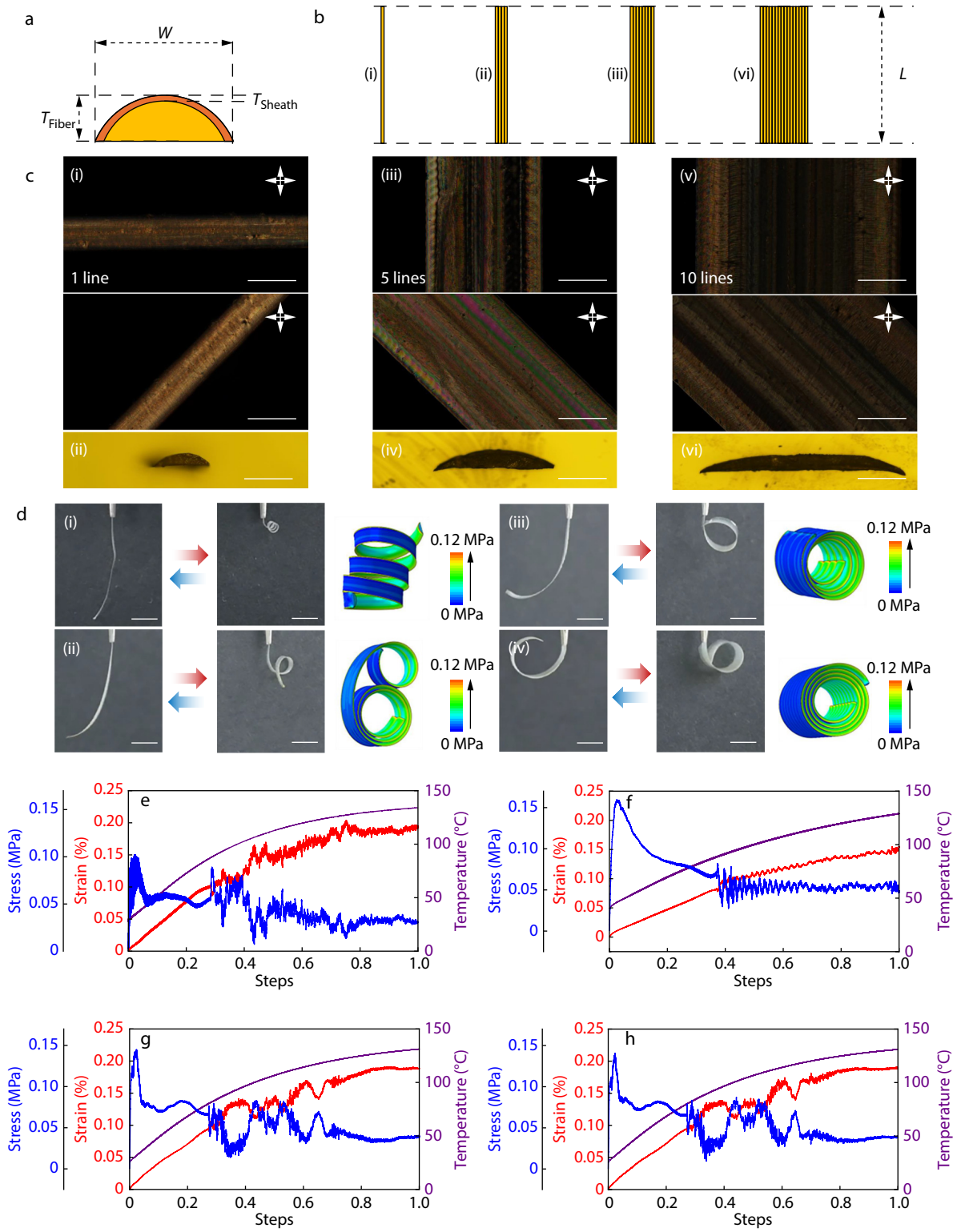

Fig. 2 Schematic illustration of (a) the core-shell structure and (b) constituent filaments of the printed samples, where (i) contains 1 filament, (ii) contains 5 filaments, (iii) contains 10 filaments, (iv) contains 20 filaments. (c) POM images and cross-sectional structures of the printed samples, where (i) and (ii) contain 1 filament, (iii) and (iv) contain 5 filaments, (v) and (vi) contain 10 filaments. Scale bar: 500 μm. (d) Reversible deformation of the printed samples upon heating, along with the corresponding finite element simulation results, where (i), (ii), (iii), and (iv) contain 1, 5, 10, and 20 filaments, respectively. Scale bar: 5 mm. The color bar of FEA model indicates the stress distribution in deformed structures, from 0.00 MPa to 0.12 MPa. The variations in stress (blue), strain (red), and temperature (purple) at specific points in FEA models during the deformation process, where (e), (f), (g), and (h) contain 1, 5, 10, and 20 filaments, respectively.

https://doi.org/10.1007/s10118-025-3288-8

numbers of filaments, with each filament having an identical core-sheath structure and the same α value. As the temperature increased, the deformation of the model became consistent with the experimental results. The FEA models in Fig. 2(d) show the stress distribution in deformed helical structures. It can be observed that the inner regions of the helical structures, that is, the sheath areas, experienced higher stress, whereas the outer regions showed lower stress owing to smaller deformation displacements. Figs. 2(e) and 2(f) illustrate the variations in the stress (blue), strain (red), and temperature (purple) at specific points in these FEA models throughout the deformation process. At the initial stage of deformation, the stress in the FEA models first increased rapidly and then experienced a sharp drop with a stress peak at approximately 30 °C. In the subsequent stage of deformation, the stress decreases slowly according to a fluctuating curve and eventually maintains a constant value. The stress change with the steps of the FEA models was consistent with the loss modulus change with the temperature of the LCEs (Fig. S1 in ESI), which was set as the temperature-dependent parameter in the FEA simulation. Therefore, the stress peaks in the FEA simulation results were presumably associated with the glass transition of the LCEs. For the FEA model consisting of a single filament, the final stress in the deformed structure is 0.03 MPa, with a strain of 0.19%. When the model consists of five filaments, uneven bending occurs, and the final stress in the deformed structure is 0.05 MPa, with a strain of 0.15%. For models consisting of 10 and 20 filaments, similar uniform bending deformations are observed, with the final stress reaching 0.04 MPa and the strain reaching 0.19% for the deformed structures.

The thermal deformation of the printed samples may have been influenced by the filament diameter. Therefore, in this study, we employed four different nozzle sizes: 1.2 mm (16G), 0.84 mm (18G), 0.34 mm (24G), and 0.21 mm (27G), to fabricate single-fibers of varying widths, as shown in Figs. 3(a) and 3(b). As shown in Fig. 3(c), increasing the nozzle diameter resulted in a wider fiber. Similar to the samples with different filament counts, the internal stress within the material increases with width, causing the as-printed actuators to lose their straight configuration at room temperature. In contrast to the as-printed samples with multiple filaments exhibiting a bending configuration, the as-printed single-filament samples were more inclined to form a helical structure as the width increased (Video S2 in ESI). As shown in Fig. 3(c), as the aspect ratio decreased, the fiber gradually transitioned from helical to bending deformation. The FEA-simulated structures exhibited a trend similar to that of the experimental structures. The α values and specific dimensional parameters of the FEA models are provided in Tables S2 and S4 (in ESI). All models had the same α value, with the only difference being the width of the models. Fig. 3(d) illustrates the temporal variation of stress (blue), strain (red), and temperature (purple) at specific points for models with widths of 250 and 1000 μm, whereas the FEA-simulated stress and strain data for a model with a width of 500 μm is shown in Fig. 2(e). Models with widths of 250 and 500 μm exhibited helical deformation with similar final stress (0.03 MPa) and strain (0.19%). While, the model with a width of 1000 μm formed a more looser wound helix, resulting in a reduced strain of 0.17% and an increased stress of 0.05 MPa.

In addition to the actuator width, thickness is a crucial factor that influences deformation behavior. Using a 0.34 mm nozzle, we printed fibers with a length of 2 cm and thicknesses of 80, 100, and 200 μm at a constant speed of 5 mm·min^{-1}, as shown in Fig. 4(a). As illustrated in Fig. 4(b), thinner samples were more susceptible to residual stress, resulting in (i) an 80 μm-thick as-printed fiber exhibiting a helical shape at room temperature. As the thickness increases, (ii) the 100 μm-thick fiber adopts a slightly bent configuration, whereas (iii) the 200 μm-thick fibers present a single-coil shape. Upon heating, the 80 μm-thick fiber undergoes a handedness-reversion from a right-handed helix to a left-handed helix, and the 100 μm-thick fiber reversibly transitions into a helical structure, whereas the 200 μm-thick fiber undergoes a coiling-reversion from clockwise coiling to anticlockwise coiling (Video S3 in ESI).

To further validate the influence of varying the thickness on the fiber deformation, we designed a structure with a thinner upper section and thicker lower section on the same fiber by adjusting the distance between the nozzle and the printing platform. The upper region had a thickness of 80 μm, whereas the lower region was 200 μm thick, as shown in Fig. 4(c). Based on the above investigation of the effect of thickness on fiber deformation, we anticipate that upon heating, the thinner upper region will exhibit helical deformation, whereas the thicker lower region will undergo bending or coiling deformation. As shown in Fig. 4(d), the thinner section of the fiber initially exhibits a loose helical structure, whereas the thicker section shows slight bending, which is consistent with previously observed experimental phenomena. Upon heating, the thinner section first undergoes helix-loosening deformation and then helix-tightening deformation, while the thicker section undergoes bending deformation. After the heat source was removed, the fiber returned to its original shape (Video S4 in ESI). The α value and specific dimensional parameters of the FEA models are listed in Tables S2 and S5 (in ESI). Figs. 4(e) and 4(f) present the stress (blue), strain (red), and temperature (purple) variation curves at specific points for the FEA models with thicknesses of 80 and 200 μm. By analyzing together with the FEA simulation result of the model with thickness of 100 μm (Fig. 2e), the FEA models with different thicknesses exhibited comparable strains (0.2%) and balanced stress (0.03 MPa).

Owing to the constraints of the glass substrate, the printed fibers undergo an anisotropic deswelling process, which leads to the formation of an anisotropic core-sheath structure, thereby causing helical deformation[39]. To investigate the influence of the core-sheath structure on the deformation behavior, we prepared fibers with a strong asymmetric core-sheath structure (glass as the printing substrate), weak asymmetric core-sheath structure (paper as the printing substrate), and symmetrical core-sheath structure (mechanical stretching). POM images of these fibers with different cross-sectional structures are shown in Fig. S3 (in ESI). For the glass substrate, the solvent can only evaporate from the air-exposed side of the fiber actuator owing to the anisotropic deswelling effect,[40, 41] leading to the formation of a highly compressed

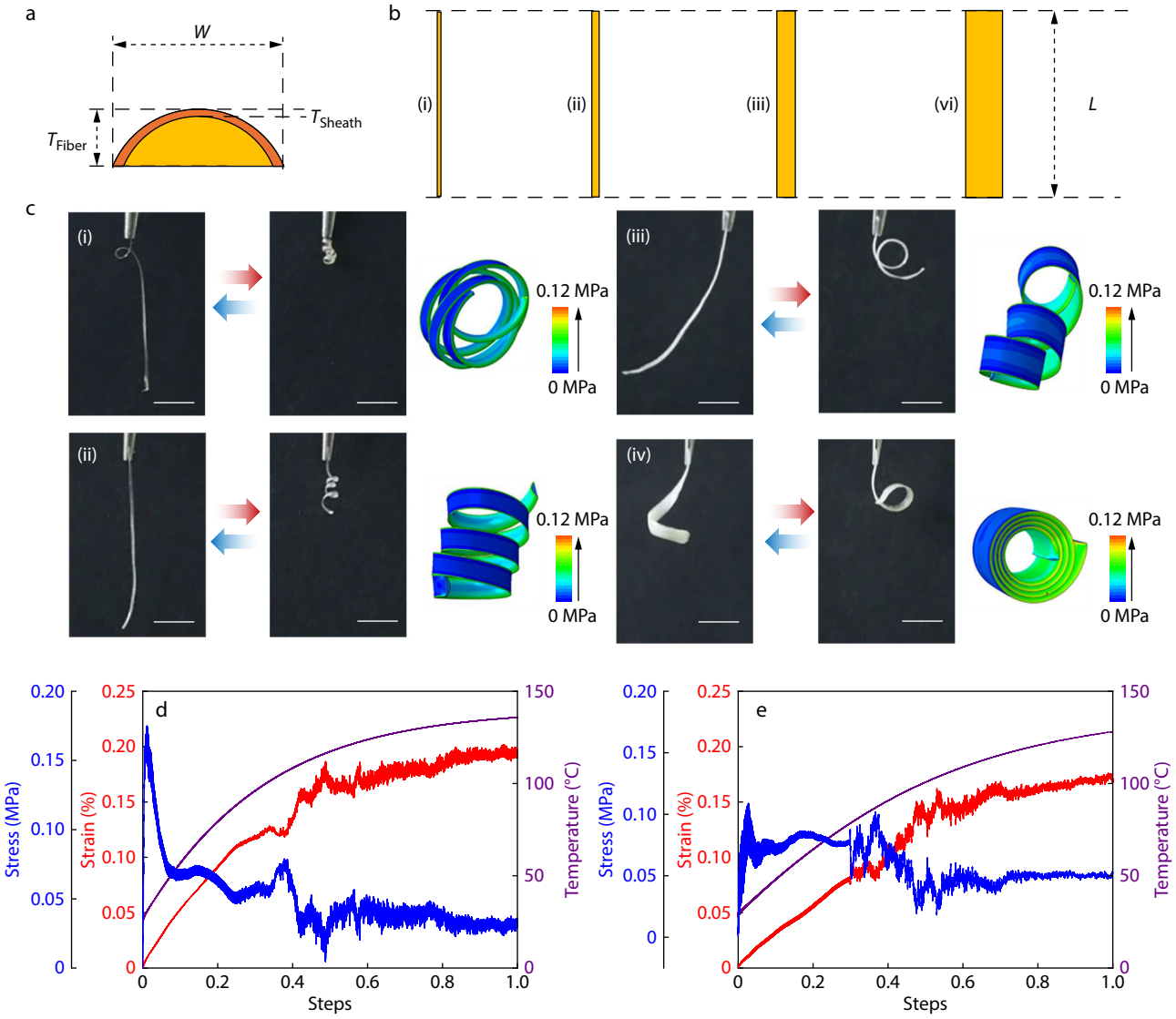

Fig. 3 (a) Schematic illustration of (a) the core-shell structure and (b) the printed samples with single filament. (c) Reversible deformation of the printed samples upon heating, along with the corresponding finite element simulation results. Scale bar: 5 mm. The color bar of FEA model indicates the stress distribution in deformed structures, from 0.00 MPa to 0.12 MPa. The variations in stress (blue), strain (red), and temperature (purple) at specific points during the deformation process of FEA models with widths of (d) 250 μm and (e) 1000 μm.

and ordered mesogen alignment on the surface of the printed fiber. In contrast, the LCE molecular chains inside the fiber experience slower solvent evaporation, providing more time for the thermal relaxation of the polymer chains to cause a looser and less ordered mesogen alignment. Consequently, the sheath and core layers exhibited significant differences in orientation, forming a strongly asymmetric core-sheath structure. When the substrate is paper, the solvent evaporates from both the air-exposed side and paper-contacted side, which reduces the orientation difference between the sheath and core layers and results in a weak asymmetric core-sheath structure.

Fig. 5(a) shows the illustration of the single-fiber actuators (i) without a core-sheath structure, (ii) with a weak asymmetric core-sheath structure and (iii) with a strong asymmetric core-sheath structure. In Fig. 5(b), (i) the mechanically stretched fibers exhibit reversible contraction-extension behavior upon heating and cooling; (ii) the fibers with a weaker core-sheath structure form a more relaxed helical configuration, whereas those with a stronger core-sheath structure generate a uniform and tightly coiled helical structure (iii). Once the heat source was removed, the fibers returned to their original state (Video S5 in ESI). Figs. 5(c) and 5(d) show the variations in the stress and strain at specific points in the FEA models. These models have the same dimensions, but different values of α. The α values for the different core-sheath structures are listed in Table S6 (in ESI), whereas the dimensional parameters are listed in Table S7 (in ESI). The FEA models without a core-sheath structure, that is, a uniform α value, exhibit contraction deformation, with the strain increasing smoothly and the stress eventually decreasing to near zero (Fig. 5c). In contrast, for the model with a weak asymmetric core-sheath structure, both the strain and deformation were smaller than those of the model with a strong

https://doi.org/10.1007/s10118-025-3288-8

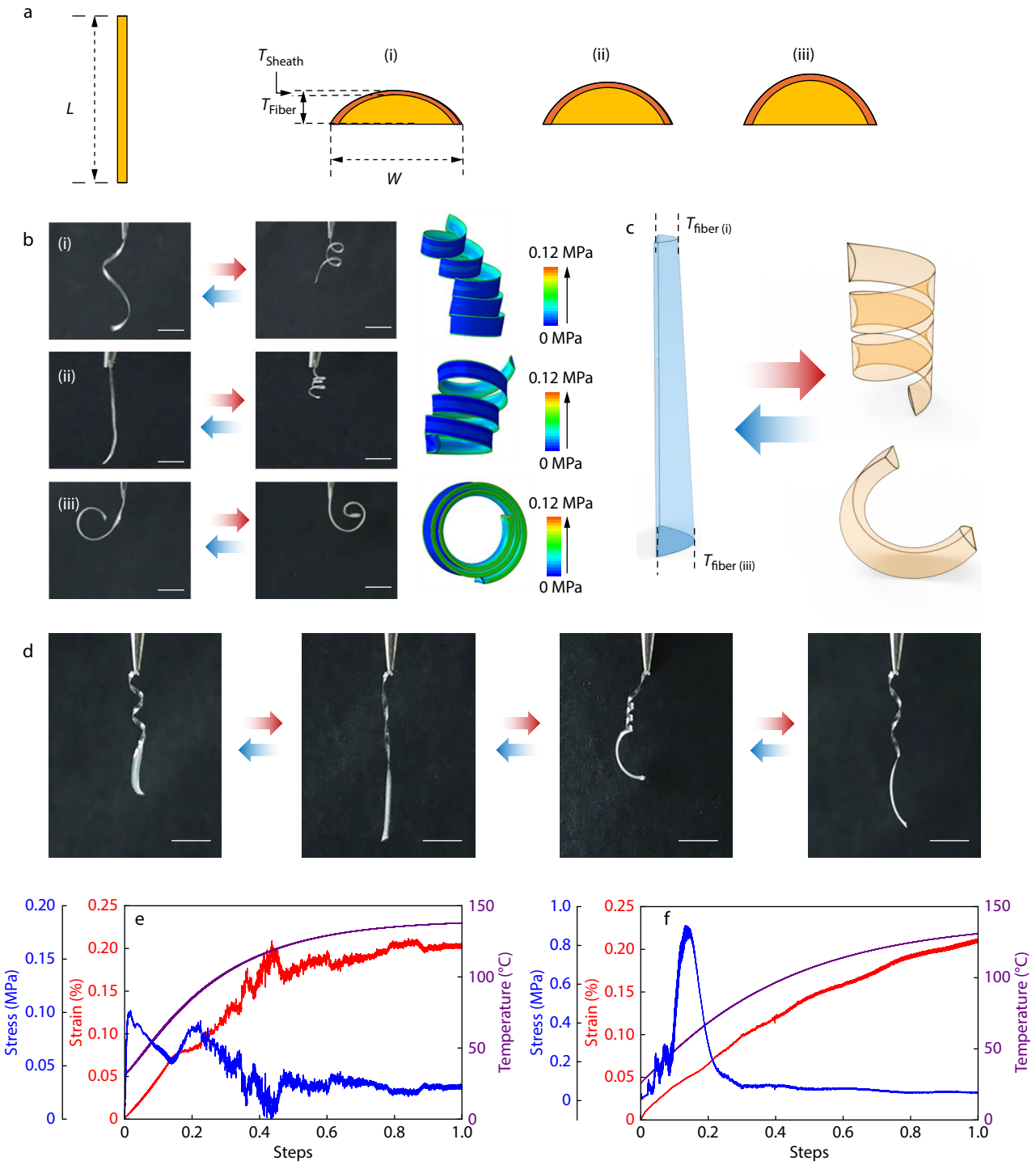

Fig. 4 (a) The single-fiber actuators with varying thicknesses, including (i) 80 μm, (ii) 100 μm, and (iii) 200 μm. (b) Reversible deformation of the printed samples upon heating and cooling, along with the corresponding finite element simulation results. Scale bar: 5 mm. The color bar of FEA model indicates the stress distribution in deformed structures, from 0.00 MPa to 0.12 MPa. (c) Schematic illustration of a single-fiber actuator with varying thickness and its deformation behavior. (d) Reversible deformation of the printed samples upon heating and cooling, where the thin upper region undergoes a helical transformation, and the thick lower region exhibits a bending deformation. Scale bar: 5 mm. The variations in stress (blue), strain (red), and temperature (purple) at specific points during the deformation process of the FEA models with thicknesses of (e) 80 μm and (f) 200 μm.

asymmetric core-sheath structure (Fig. 2e). It should be noted that there are both similarities and differences in the helical deformation mechanism between the natural plant tendrils and our fiber actuators. Similarly, both natural plant tendrils and our fiber actuators possess a core-sheath structure, and the formation of their helical structures is attributed to asym-

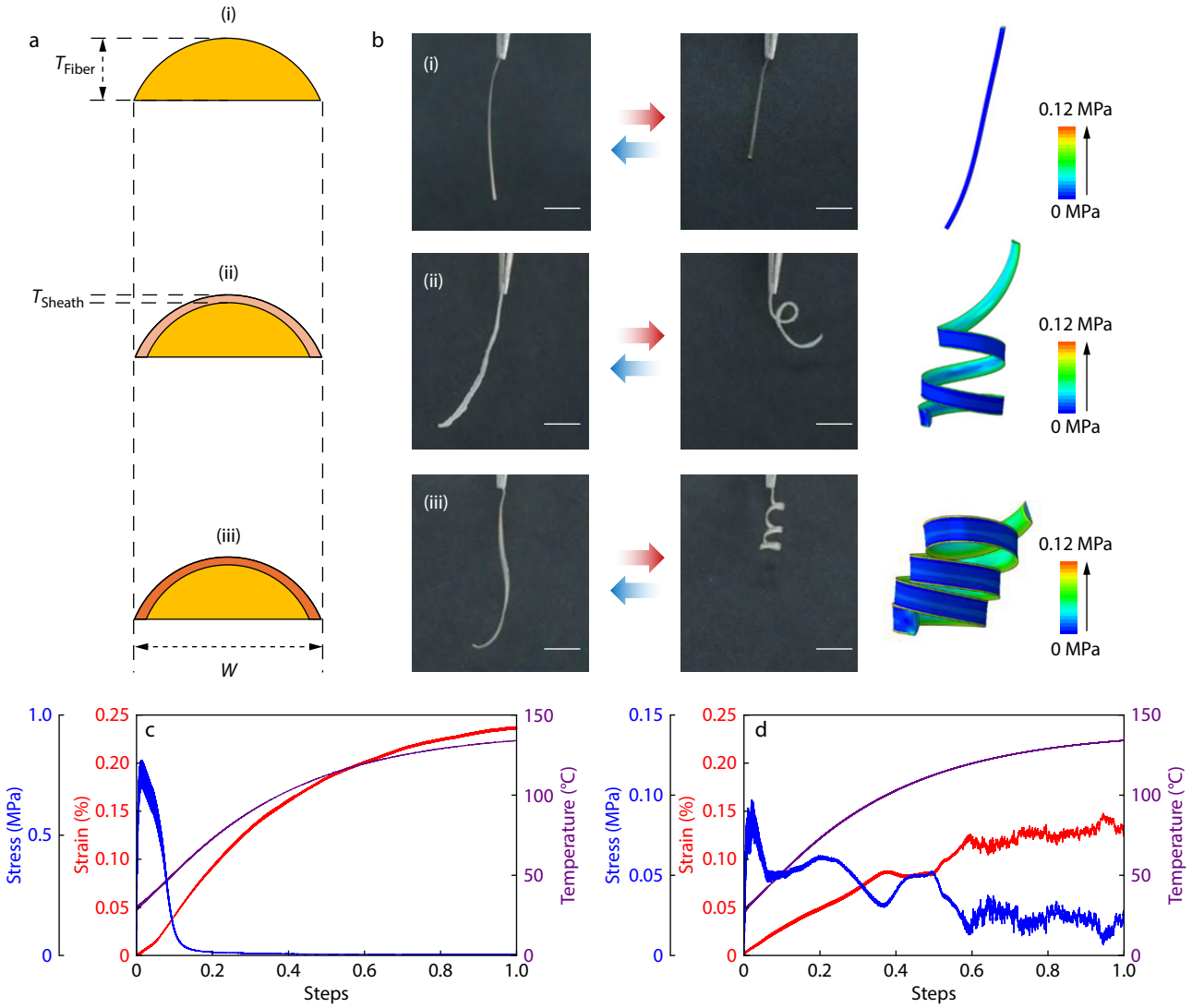

Fig. 5 (a) Schematic illustration of the single-fiber actuators (i) without a core-sheath structure, (ii) with a weak asymmetric core-sheath structure and (iii) with a strong asymmetric core-sheath structure. (b) Reversible deformation of the printed samples upon heating and cooling, along with the corresponding finite element simulation results. Scale bar: 5 mm. The color bar of FEA model indicates the stress distribution in deformed structures, from 0.00 MPa to 0.12 MPa. The variations in stress (blue), strain (red), and temperature (purple) at specific points during the deformation process of the FEA models (c) without a core-sheath structure and (d) with a weak asymmetric core-sheath structure.

metric contraction. In contrast, in plant tendrils, helical structures are caused by the lignification of specialized structural gelatinous fiber cells and their asymmetric contractions along the length. In contrast, for fiber actuators, helical deformations result from the differences in the orientation of mesogens in the sheath and core layers, which can lead to differential contractions between the sheath and core layers upon heating.

CONCLUSIONS

In summary, using a two-step aza-Michael addition reaction, we successfully fabricated fiber-based actuators with various three-dimensional structures and asymmetric core-sheath configurations *via* DIW 4D printing technology. High-aspect-ratio LCE fiber-based actuators with a core-sheath alignment structure exhibit helical deformation upon heating driven by asymmetric contraction. The influence of dimensional parameters and core-sheath structures on the helical deformation behavior was investigated using finite element simulations, and the mechanism of helical deformations of the LCE fiber actuators was revealed by a detailed analysis of the FEA-simulated stress and strain variation during the deformation process. The study revealed that the printing speed, nozzle diameter, and printing path significantly influence the morphology and alignment of the fiber actuators. By precisely adjusting these printing parameters, we can control the fiber width, filament number, thickness, and core-sheath structure, thus modulating the helical deformation behavior. Owing to the residual stress, fiber-based actuators exhibit straight, helical, or coiling shapes at room temperature. Upon heating, as the aspect ratio and thickness increased, the deformation gradually transitioned from helical to coiled and/or bent. These findings demonstrate that the precise tuning of printing parameters allows not only the control of LCE

https://doi.org/10.1007/s10118-025-3288-8

fiber morphology but also the customization of their functional properties, providing a solid theoretical foundation and technical support for applications in smart materials, biomedical engineering, and flexible electronics.

Conflict of Interests

The authors declare no interest conflict.

Electronic Supplementary Information

Electronic supplementary information (ESI) is available free of charge in the online version of this article at http://doi.org/10.1007/s10118-025-3288-8.

Data Availability Statement

The data that support the findings of this study are available from the corresponding author upon reasonable request. The author's contact information: xililu@scu.edu.cn.

ACKNOWLEDGMENTS

This work was financially supported by the National Natural Science Foundation of China (Nos. 52103145 and 11832007), Science & Technology Department of Sichuan Province (No. 2025ZNSFSC0352), and State Key Laboratory of Polymer Materials Engineering (No. sklpme-2024-1-03).

REFERENCES

1 White, T. J.; Broer, D. J. Programmable and adaptive mechanics with liquid crystal polymer networks and elastomers. *Nat. Mater.* **2015**, *14*, 1087–1098.
2 Herbert, K. M.; Fowler, H. E.; McCracken, J. M.; Schlafmann, K. R.; Koch, J. A.; White, T. J. Synthesis and alignment of liquid crystalline elastomers. *Nat. Rev. Mater.* **2021**, *7*, 23–38.
3 Ware, T. H.; McConney, M. E.; Wie, J. J.; Tondiglia, V. P.; White, T. J. Voxelated liquid crystal elastomers. *Science* **2015**, *347*, 982–984.
4 Nie, Z. Z.; Wang, M.; Huang, S.; Liu, Z. Y.; Yang, H. Multimodal self-sustainable autonomous locomotions of light-driven Seifert ribbon actuators based on liquid crystal elastomers. *Angew. Chem. Int. Ed.* **2023**, *62*, e202304081.
5 Boothby, J. M.; Gagnon, J. C.; McDowell, E.; Van Volkenburg, T.; Currano, L.; Xia, Z. Y. An untethered soft robot based on liquid crystal elastomers. *Soft Robot.* **2022**, *9*, 154–162.
6 Guin, T.; Settle, M. J.; Kowalski, B. A.; Auguste, A. D.; Beblo, R. V.; Reich, G. W.; White, T. J. Layered liquid crystal elastomer actuators. *Nat. Commun.* **2018**, *9*, 2531.
7 Ohm, C.; Brehmer, M.; Zentel, R. Liquid crystalline elastomers as actuators and sensors. *Adv. Mater.* **2010**, *22*, 3366–3387.
8 Hou, W. H.; Wang, J.; Lv, J. A. Bioinspired liquid crystalline spinning enables scalable fabrication of high-performing fibrous artificial muscles. *Adv. Mater.* **2023**, *35*, 2211800.
9 Kim, I. H.; Choi, S.; Lee, J.; Jung, J.; Yeo, J.; Kim, J. T.; Ryu, S.; Ahn, S. K.; Kang, J.; Poulin, P.; Kim, S. O. Human-muscle-inspired single fibre actuator with reversible percolation. *Nat. Nanotechnol.* **2022**, *17*, 1198–1205.
10 Zhou, X. R.; Jin, B. J.; Zhu, Z.; Wu, J. J.; Zhao, Q.; Chen, G. C. Metal-ligand bonds based reprogrammable and re-processable supramolecular liquid crystal elastomer network. *Angew. Chem. Int. Ed.* **2024**, *63*, e202409182.
11 Zeng, H.; Wani, O. M.; Wasylczyk, P.; Kaczmarek, R.; Priimagi, A. Self-regulating iris based on light-actuated liquid crystal elastomer. *Adv. Mater.* **2017**, *29*, 1701814.
12 Turiv, T.; Krieger, J.; Babakhanova, G.; Yu, H.; Shiyanovskii, S. V.; Wei, Q. H.; Kim, M. H.; Lavrentovich, O. D. Topology control of human fibroblast cells monolayer by liquid crystal elastomer. *Sci. Adv.* **2020**, *6*, eaaz6485.
13 Fu, P.; Li, H. M.; Gong, J.; Fan, Z. J.; Smith, A. T.; Shen, K. Y.; Khalfalla, T. O.; Huang, H. F.; Qian, X.; McCutcheon, J. R.; Sun, L. Y. 4D printing of polymers: techniques, materials, and prospects. *Prog. Polym. Sci.* **2022**, *126*, 101506.
14 Ghazal, A. F.; Zhang, M.; Mujumdar, A. S.; Ghamry, M. Progress in 4D/5D/6D printing of foods: applications and R&D opportunities. *Crit. Rev. Food Sci. Nutr.* **2023**, *63*, 7399–7422.
15 Zhou, X. L.; Ren, L. Q.; Song, Z. Y.; Li, G. W.; Zhang, J. F.; Li, B. Q.; Wu, Q.; Li, W. X.; Ren, L.; Liu, Q. P. Advances in 3D/4D printing of mechanical metamaterials: from manufacturing to applications. *Compos. Part B Eng.* **2023**, *254*, 110585.
16 Guan, Z. C.; Wang, L.; Bae, J. Advances in 4D printing of liquid crystalline elastomers: materials, techniques, and applications. *Mater. Horiz.* **2022**, *9*, 1825–1849.
17 Chen, M.; Gao, M.; Bai, L. C.; Zheng, H.; Qi, H. J.; Zhou, K. Recent advances in 4D printing of liquid crystal elastomers. *Adv. Mater.* **2023**, *35*, 2209566.
18 del Pozo, M.; Sol, J. A. H. P.; Schenning, A. P. H. J.; Debije, M. G. 4D printing of liquid crystals: What's right for me? *Adv. Mater.* **2022**, *34*, 2104390.
19 Wan, X.; Luo, L.; Liu, Y. J.; Leng, J. S. Direct ink writing based 4D printing of materials and their applications. *Adv. Sci.* **2020**, *7*, 2001000.
20 Wang, Q. R.; Tian, X. Y.; Zhang, D. K.; Zhou, Y. L.; Yan, W. Q.; Li, D. C. Programmable spatial deformation by controllable off-center freestanding 4D printing of continuous fiber reinforced liquid crystal elastomer composites. *Nat. Commun.* **2023**, *14*, 3869.
21 Zhai, F.; Feng, Y. Y.; Li, Z. Y.; Xie, Y. X.; Ge, J.; Wang, H.; Qiu, W.; Feng, W. 4D-printed untethered self-propelling soft robot with tactile perception: rolling, racing, and exploring. *Matter*, **2021**, *4*, 3313–3326.
22 Ambulo, C. P.; Burroughs, J. J.; Boothby, J. M.; Kim, H.; Ravi Shankar, M.; Ware, T. H. Four-dimensional printing of liquid crystal elastomers. *ACS Appl. Mater. Interfaces* **2017**, *9*, 37332–37339.
23 Kotikian, A.; McMahan, C.; Davidson, E. C.; Muhammad, J. M.; Weeks, R. D.; Daraio, C.; Lewis, J. A. Untethered soft robotic matter with passive control of shape morphing and propulsion. *Sci. Robot.* **2019**, *4*, eaax7044.
24 Zhang, C.; Lu, X. L.; Fei, G. X.; Wang, Z. H.; Xia, H. S.; Zhao, Y. 4D printing of a liquid crystal elastomer with a controllable orientation gradient. *ACS Appl. Mater. Interfaces* **2019**, *11*, 44774–44782.
25 Ren, L. Q.; Li, B. Q.; He, Y. L.; Song, Z. Y.; Zhou, X. L.; Liu, Q. P.; Ren, L. Programming shape-morphing behavior of liquid crystal elastomers *via* parameter-encoded 4D printing. *ACS Appl. Mater. Interfaces* **2020**, *12*, 15562–15572.
26 Wang, Z. J.; Wang, Z. J.; Zheng, Y.; He, Q. G.; Wang, Y.; Cai, S. Q. Three-dimensional printing of functionally graded liquid crystal elastomer. *Sci. Adv.* **2020**, *6*, eabc0034.
27 Liang, H.; Liu, Y. W.; Xu, H. T.; Yang, Y.; He, E. J.; Yang, Z. J.; Wei, Y.; Ji, Y. Thiol-acrylate catalyst enabled post-synthesis fabrication of liquid crystal actuators. *Chinese J. Polym. Sci.*, **2023**, *41*, 1656-1662.
28 Sun, J. H.; Liao, W.; Yang, Z. Q. Additive manufacturing of liquid crystal elastomer actuators based on knitting technology. *Adv.*

Mater. **2023**, *35*, 2302706.
29 Gerbode, S. J.; Puzey, J. R.; McCormick, A. G.; Mahadevan, L. How the cucumber tendril coils and overwinds. *Science* **2012**, *337*, 1087–1091.
30 Hu, Z. M.; Li, Y. L.; Lv, J. A. Phototunable self-oscillating system driven by a self-winding fiber actuator. *Nat. Commun.* **2021**, *12*, 3211.
31 Farahani, R. D.; Chizari, K.; Therriault, D. Three-dimensional printing of freeform helical microstructures: a review. *Nanoscale* **2014**, *6*, 10470–10485.
32 Wang, Y. P.; Sun, J. H.; Liao, W.; Yang, Z. Q. Liquid crystal elastomer twist fibers toward rotating microengines. *Adv. Mater.* **2022**, *34*, 2107840.
33 Lugger, S. J. D.; Engels, T. A. P.; Cardinaels, R.; Bus, T.; Mulder, D. J.; Schenning, A. P. H. J. Melt-extruded thermoplastic liquid crystal elastomer rotating fiber actuators. *Adv. Funct. Mater.* **2023**, *33*, 2306853.
34 Cui, B.; Ren, M.; Dong, L. Z.; Wang, Y. L.; He, J. F.; Wei, X. L.; Zhao, Y. R.; Xu, P. P.; Wang, X. N.; Di, J. T.; Li, Q. W. Pretension-free and self-recoverable coiled artificial muscle fibers with powerful cyclic work capability. *ACS Nano* **2023**, *17*, 12809–12819.
35 Chen, Z.; Majidi, C.; Srolovitz, D. J.; Haataja, M. Tunable helical ribbons. *Appl. Phys. Lett.* **2011**, *98*, 011906.
36 Armon, S.; Efrati, E.; Kupferman, R.; Sharon, E. Geometry and mechanics in the opening of chiral seed pods. *Science* **2011**, *333*, 1726–1730.
37 Sawa, Y.; Ye, F. F.; Urayama, K.; Takigawa, T.; Gimenez-Pinto, V.; Selinger, R. L. B.; Selinger, J. V. Shape selection of twist-nematic-elastomer ribbons. *Proc. Natl. Acad. Sci. USA* **2011**, *108*, 6364–6368.
38 Yin, L.; Miao, T. F.; Cheng, X. X.; Jiang, Z. C.; Tong, X.; Zhang, W.; Zhao, Y. Chiral liquid crystalline elastomer for twisting motion without preset alignment of mesogens. *ACS Macro Lett.* **2021**, *10*, 690–696.
39 Zhang, C.; Fei, G. X.; Lu, X. L.; Xia, H. S.; Zhao, Y. Liquid crystal elastomer artificial tendrils with asymmetric core–sheath structure showing evolutionary biomimetic locomotion. *Adv. Mater.* **2024**, *36*, 2307210.
40 Kim, S. T.; Finkelmann, H. Cholesteric liquid single-crystal elastomers (LSCE) obtained by the anisotropic deswelling method. *Macromol. Rapid Commun.* **2001**, *22*, 429–433.
41 Kizhakidathazhath, R.; Geng, Y.; Jampani, V. S. R.; Charni, C.; Sharma, A.; Lagerwall, J. P. F. Facile anisotropic deswelling method for realizing large-area cholesteric liquid crystal elastomers with uniform structural color and broad-range mechanochromic response. *Adv. Funct. Mater.* **2020**, *30*, 1909537.

https://doi.org/10.1007/s10118-025-3288-8